Minimizing the fluctuation of resonance driving terms in dynamic aperture optimization

Bingfeng Wei,[1] Zhenghe Bai,[1,2,*] Jiajie Tan,[1] Lin Wang,[1] and Guangyao Feng[1,†]

[1]*National Synchrotron Radiation Laboratory, University of Science and Technology of China, Hefei 230029, China*

[2]*Synchrotron SOLEIL, L'Orme des Merisiers, 91190 Saint-Aubin, France*

(Received 28 March 2023; accepted 24 July 2023; published 9 August 2023)

Dynamic aperture (DA) is an important nonlinear property of a storage ring lattice, which has a dominant effect on beam injection efficiency and beam lifetime. Generally, minimizing both resonance driving terms (RDTs) and amplitude dependent tune shifts is an essential condition for enlarging the DA. In this paper, we study the correlation between the fluctuation of RDTs along the longitudinal position and the DA area with double-bend and multibend achromat lattices. The fluctuation of one RDT is quantitatively represented by the average RDT at the positions of nonlinear magnets. It is found that minimizing the RDT fluctuations is more effective than minimizing the commonly-used one-turn RDTs in enlarging the DA, and thus can serve as a very powerful indicator in the DA optimization. It is also found that minimizing low-order RDT fluctuations can also reduce both higher-order one-turn RDTs and higher-order RDT fluctuations, which also indicates that even higher-order RDTs can also be controlled due to the reduction of higher-order RDT fluctuations. This could be the underlying physics behind the strong correlation between minimizing the RDT fluctuations and enlarging the DA. And this also suggests that controlling lower-order RDT fluctuations in the DA optimization can avoid the need for calculating higher-order RDTs to a large extent, which are not only more computationally complicated but also more numerous. Besides, the effectiveness of controlling the RDT fluctuations in enlarging the DA confirms that the local cancellation of nonlinear effects used in some diffraction-limited storage ring lattices is more effective than the global cancellation.

DOI: 10.1103/PhysRevAccelBeams.26.084001

I. INTRODUCTION

Dynamic aperture (DA) has a dominant effect on beam injection efficiency and beam lifetime of a storage ring. Optimization of the DA is a complex problem with a long history. In the past decade or so, due to the improvement of computer performance and the application of evolutionary algorithms, particle tracking-based numerical approach has been widely used for DA optimization, in which genetic algorithm or particle swarm optimization algorithm is applied to find the globally best solution [1–6]. But this numerical approach is quite demanding in computational resources, and in general, there is basically no physics to guide further lattice optimization. As an alternative and complementary approach, resonance driving term (RDT) minimization [7] is a traditional analytical approach with fast optimization speed and easily-revealed physics. In this analytical approach, minimizing RDTs to suppress the corresponding resonances and also controlling amplitude dependent tune shifts (ADTS) to avoid resonance crossings can help to enlarge the DA. However, small RDTs is a necessary but not sufficient condition for large DA [2], and the optimization result obtained by this approach largely depends on the lattice designers' experiences.

Nevertheless, the guidance of the RDTs is of great significance. Two types of nonlinear cancellation schemes, which are made within one lattice cell, were proposed in the multibend achromat (MBA) lattice design of diffraction-limited storage rings (DLSRs) and showed remarkable success [8,9]. One is the hybrid MBA lattice with a pair of $-\mathcal{I}$ separated dispersion bumps [8], and the other is the higher-order achromat (HOA) lattice with some identical bend unit cells [9]. Both can cancel the main RDTs generated by sextupoles within one lattice cell. This local cancellation prevents the RDTs from building up along the ring and is thus more effective than the global cancellation made over some lattice cells [10]. This inspires us the importance of suppressing the variation or fluctuation of

*Corresponding author.
baizhe@ustc.edu.cn

†Corresponding author.
fenggy@ustc.edu.cn

RDTs in improving the nonlinear dynamics. In this paper, the RDTs of nonlinear magnets will be calculated as a function of the longitudinal position. There are two ways to show the fluctuation of RDTs along the longitudinal position. One is to calculate the accumulated RDTs from a fixed longitudinal starting position, the same as in Refs. [11,12] and similar to the calculation of multiperiod RDTs in OPA [13]. This way can show the build-up and cancellation of RDTs, and here we call it the build-up fluctuation of RDTs. The other is to calculate one-period or one-turn RDTs with varying longitudinal starting position, which was presented in Refs. [14–17] and also used in ELEGANT [18]. We will discuss these two kinds of RDT fluctuations in this paper, and try to find the correlation between the DA area and the RDT fluctuations with a large number of nonlinear lattice solutions. We noticed that in Ref. [19], the turn-by-turn fluctuations of the Courant-Snyder actions were minimized to enlarge the DA.

The remaining sections of this paper are outlined as follows. Section II introduces the RDTs briefly, and describes two kinds of RDT fluctuations and give the correlation between them. We also analyze the relation between reducing RDT fluctuations and control of crossing terms of nonlinear magnets, which is beneficial for enlarging the DA. Then, in Sec. III, the study starts with the simple double-bend achromat (DBA) lattice of a third-generation synchrotron light source, where low-order RDTs are the most important. Next we step further into the more complex case of two 6BA lattices of DLSRs in Sec. IV. At the end of the paper, a brief summary and outlook are given.

II. CONTROL OF THE RDT FLUCTUATIONS

The one-turn map of a storage ring with $N+1$ linear maps separated by N thin-lens sextupole maps can be normalized as [7]:

$$\begin{aligned}\mathcal{M}_{0\to N+1} &= \mathcal{M}_{0\to 1}e^{:V_1:}\mathcal{M}_{1\to 2}e^{:V_2:}\ldots e^{:V_N:}\mathcal{M}_{N\to N+1}\\ &= \mathcal{A}_0^{-1}e^{:\hat{V}_1:}e^{:\hat{V}_2:}\ldots e^{:\hat{V}_N:}\mathcal{R}_{0\to N+1}\mathcal{A}_{N+1}\\ &= \mathcal{A}_0^{-1}e^{:h:}\mathcal{R}_{0\to N+1}\mathcal{A}_{N+1},\end{aligned} \tag{1}$$

where $\hat{V}_i \equiv \mathcal{R}_{0\to i}\mathcal{A}_i V_i$, $\mathcal{A}$ is a normalizing map, $\mathcal{R}$ is a rotation, and $e^{:h:}$ is the nonlinear Lie map. Using the resonance basis, the nth order generator of $e^{:h:}$ can be expanded as:

$$h_n = \sum_{n=j+k+l+m+p} h_{jklmp}h_x^{+j}h_x^{-k}h_y^{+l}h_y^{-m}\delta^p, \tag{2}$$

where $h_x^{\pm} \equiv \sqrt{2J_x}e^{\pm i\phi_x}$, $h_y^{\pm} \equiv \sqrt{2J_y}e^{\pm i\phi_y}$, with (J,ϕ) being action-angle variables, and h_{jklmp} is the so-called driving terms. The terms with $p \neq 0$ are chromatic terms, which affect the off-momentum dynamics. In this paper we focus on the on-momentum DA, where the geometric terms with $p=0$ are considered. The geometric terms can be divided into two categories. The terms with $j=k$ and $l=m$ drive the ADTS, and the remaining terms drive resonances $(j-k)\nu_x+(l-m)\nu_y$.

The concept of RDTs is derived from the one-turn map, and traditionally, one focuses on the RDTs of a periodic map or one-turn map. In this paper we take the fluctuation of RDTs along the longitudinal position into consideration. Denoting $\prod_{a=1}^{t} e^{:\hat{V}_a:} \equiv e^{:S_t:}$, $e^{:S_t:} = e^{:S_{t-1}:}e^{:\hat{V}_t:}$, and when $t=N$, S_N is the h of Eq. (1). According to the Baker-Campbell-Hausdorff formula [20], we have

$$\begin{aligned}S_t = S_{t-1} + \hat{V}_t + \frac{1}{2}:S_{t-1}:\hat{V}_t + \frac{1}{12}:S_{t-1}:^2\hat{V}_t\\ + \frac{1}{12}:\hat{V}_t:^2 S_{t-1} + \cdots.\end{aligned} \tag{3}$$

Equation (3) indicates that the lower-order terms of S_{t-1} contribute to the higher-order terms of S_t. Expanding S_t with the resonance basis as in Eq. (2), we can get a series of nonlinear terms that show the build-up fluctuation of driving terms h_{jklmp}. We denote the driving terms of S_t as $h_{1\to t,jklmp}$. And by expanding $\hat{V}_t$, we can get the contribution of the tth sextupole to the third-order RDTs, denoted as $h_{t,jklmp}$. For the third-order RDTs, $h_{1\to t,jklmp} = \sum_{a=1}^{t} h_{a,jklmp}$. The lower-order RDT build-up fluctuations contribute to the higher-order RDTs of the one-turn map. For example, the fourth-order RDTs of sextupoles are crossing terms of their third-order RDTs [7],

$$h_4 = \frac{1}{2}\sum_{b>a=1}^{N}[\hat{V}_a,\hat{V}_b] = \frac{1}{2}\sum_{b=2}^{N}\left[\sum_{a=1}^{b-1}\hat{V}_a,\hat{V}_b\right], \tag{4}$$

where $\sum_{a=1}^{b-1}\hat{V}_a$ is the third-order term of S_{b-1}. Reducing the amplitude of $h_{1\to t,jklmp}$ can be beneficial for controlling the crossing terms. Therefore, minimizing the RDT build-up fluctuations is beneficial for reducing the higher-order one-turn RDTs as well as higher-order RDT fluctuations. And as the higher-order RDT fluctuations decrease, the even higher-order RDTs are also controlled. This is the physics why minimizing the RDT fluctuations can be very effective in enlarging the DA, which will be demonstrated later. The analysis above can also apply to a storage ring with both sextupoles and octupoles.

The crossing terms are the key in the physical analysis above. There is an exception with thin sextupoles where no crossing term is generated [20]. The simplest case of this exception is the well-known $-\mathcal{I}$ transformation with two identical thin sextupoles at both sides. In this exception, the nonlinear effects of the thin sextupoles can cancel each other. Scaling the sextupole strengths, i.e., changing the RDT fluctuations, does not affect the nonlinear cancellation and the infinite DA. However, in the realistic lattices where sextupoles have thickness, crossing terms are always

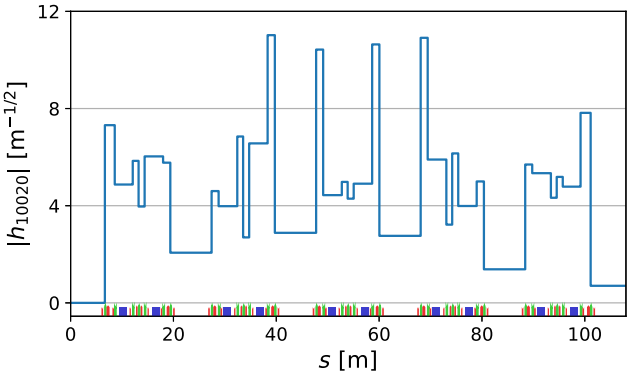

FIG. 1. The amplitude variation of the third-order RDT h_{10020} at the locations of sextupoles (green blocks in the magnet layout) in one SP of the SSRF storage ring lattice. The RDT is cumulatively calculated from zero.

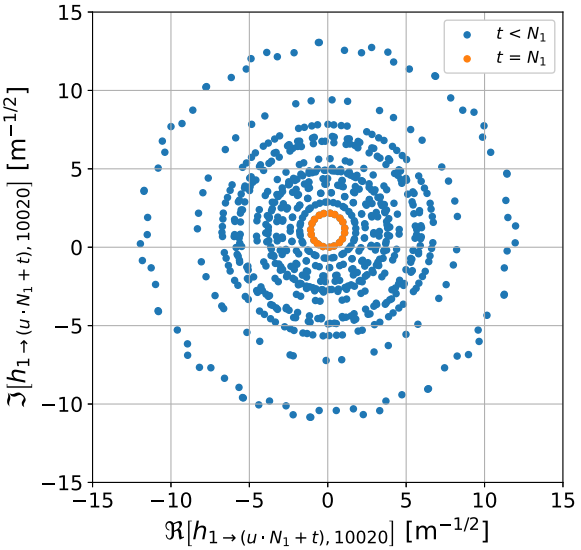

FIG. 2. Build-up fluctuation of h_{10020} of the SSRF lattice in the complex plane for 20 SPs.

present. Therefore, minimizing the RDT fluctuations can be effectively applied to the realistic lattices.

In order to clearly illustrate the build-up fluctuations of RDTs, the third-order RDT h_{10020} of the SSRF storage ring lattice is plotted in Fig. 1 as a function of position in one superperiod (SP). It changes stepwise at the locations of sextupoles. Traditionally, in order to enlarge the on-momentum DA, it is necessary to control the values of geometric RDTs of one-turn map, denoted as $h_{jklm0,\mathrm{ring}}$.

In the complex plane, we can characterize the build-up fluctuation of RDTs more clearly and show the regularity. Referring the definition in Ref. [13], we introduce $\boldsymbol{m} = (j-k, l-m)$ to represent the mode of h_{jklm0} and $\boldsymbol{\mu} = 2\pi(\nu_x, \nu_y)$ the phase advances of one SP. We can use the RDT build-up fluctuation data of one SP to construct the build-up fluctuation over any number of SPs. For each third-order RDT h_{jklm0}, if we denote the number of sextupoles of one SP as N_1, the value of h_{jklm0} at the tth sextupole of the $(u+1)$th SP $(1 \le t \le N_1, u \ge 0)$ is

$$\begin{aligned} h_{1\to(u\cdot N_1+t),jklm0} &= h_{1\to u\cdot N_1,jklm0} + h_{(u\cdot N_1+1)\to(u\cdot N_1+t),jklm0} \\ &= h_{1\to N_1,jklm0}\frac{1-e^{iu\boldsymbol{m}\cdot\boldsymbol{\mu}}}{1-e^{i\boldsymbol{m}\cdot\boldsymbol{\mu}}} + h_{1\to t,jklm0}e^{iu\boldsymbol{m}\cdot\boldsymbol{\mu}} \\ &= \frac{h_{1\to N_1,jklm0}}{1-e^{i\boldsymbol{m}\cdot\boldsymbol{\mu}}} + \left(h_{1\to t,jklm0} - \frac{h_{1\to N_1,jklm0}}{1-e^{i\boldsymbol{m}\cdot\boldsymbol{\mu}}}\right)e^{iu\boldsymbol{m}\cdot\boldsymbol{\mu}} \\ &= C_{0,\boldsymbol{m}} + C_{t,\boldsymbol{m}}e^{iu\boldsymbol{m}\cdot\boldsymbol{\mu}}, \\ \text{with}\quad C_{0,\boldsymbol{m}} &= \frac{h_{1\to N_1,jklm0}}{1-e^{i\boldsymbol{m}\cdot\boldsymbol{\mu}}}, \\ C_{t,\boldsymbol{m}} &= h_{1\to t,jklm0} - \frac{h_{1\to N_1,jklm0}}{1-e^{i\boldsymbol{m}\cdot\boldsymbol{\mu}}}. \end{aligned} \tag{5}$$

The calculation of multiperiod RDTs in Eq. (5) can be found in Ref. [13]. With u as a variable, Eq. (5) is a circle in the complex plane with $C_{0,\boldsymbol{m}}$ as its center and $|C_{t,\boldsymbol{m}}|$ as its radius. Also taking the SSRF lattice as an example, we calculated the build-up fluctuation of h_{10020} for 20 SPs, and the results are plotted in the complex plane in Fig. 2. For N_1 sextupoles, there are N_1 concentric circles as the dots shown in Fig. 2. And when $t = N_1$, the circle passes the origin as shown with the orange dots. The $C_{0,\boldsymbol{m}}$, which is the center of these circles, shows the overall offset. Traditionally, minimizing one RDT only involves $C_{0,\boldsymbol{m}}$. While reducing the build-up fluctuation of one RDT involves reducing both the radii of these circles and the offset of the center.

As for the second kind of RDT fluctuations, the definition of RDTs is different. A transformation F, which is a polynomial function, is used to find the nonlinear invariants, and these RDTs are the coefficients in F,

denoted as f_{jklm0} [17]. The phase advances between the observation position s of this fluctuation and the starting position of the build-up fluctuation are denoted as $\Delta\boldsymbol{\phi}(s) = (\Delta\phi_x(s), \Delta\phi_y(s))$. For an observation position s between the tth and $(t+1)$th sextupoles, the third-order RDT $f_{jklm0}(s)$ is

$$\begin{aligned} f_{jklm0}(s) &= \frac{h_{(t+1)\to(N_1+t),jklm0} e^{-i\boldsymbol{m}\cdot\Delta\boldsymbol{\phi}(s)}}{1-e^{i\boldsymbol{m}\cdot\boldsymbol{\mu}}} \\ &= \frac{h_{(t+1)\to N_1,jklm0} + h_{1\to t,jklm0} e^{i\boldsymbol{m}\cdot\boldsymbol{\mu}}}{1-e^{i\boldsymbol{m}\cdot\boldsymbol{\mu}}} e^{-i\boldsymbol{m}\cdot\Delta\boldsymbol{\phi}(s)} \\ &= \frac{h_{1\to N_1,jklm0} - (1-e^{i\boldsymbol{m}\cdot\boldsymbol{\mu}}) h_{1\to t,jklm0}}{1-e^{i\boldsymbol{m}\cdot\boldsymbol{\mu}}} e^{-i\boldsymbol{m}\cdot\Delta\boldsymbol{\phi}(s)} \\ &= -C_{t,\boldsymbol{m}} e^{-i\boldsymbol{m}\cdot\Delta\boldsymbol{\phi}(s)}. \end{aligned} \tag{6}$$

So $|f_{jklm0}(s)|$ is equal to $|C_{t,\boldsymbol{m}}|$ in Eq. (5), which is exactly the radius of the circle formed by the RDT build-up fluctuation. Then the values of f_{jklm0} for one period are at a series of concentric circles in the complex plane as shown in Fig. 3. The difference between these two kinds of fluctuations is that the center of circles in Fig. 2, which is also equal to $f_{jklm0}(0)$, is not at the origin. The amplitude of $f_{10020}(s)$ of the SSRF lattice is shown in Fig. 4, which is similar to Fig. 1. This is because h_{10020} is almost canceled over one SP and $C_{0,\boldsymbol{m}}$ in Eq. (5) is small. For the third-order RDTs, minimizing $|C_{t,\boldsymbol{m}}|$ is helpful for controlling both of the two kinds of fluctuations.

The case of the fourth-order RDTs is similar but more complex. As shown in Appendix A, the values of fourth-order $f_{jklm0}(s)$ are also at a series of concentric circles in the complex plane. The radii of these circles are the

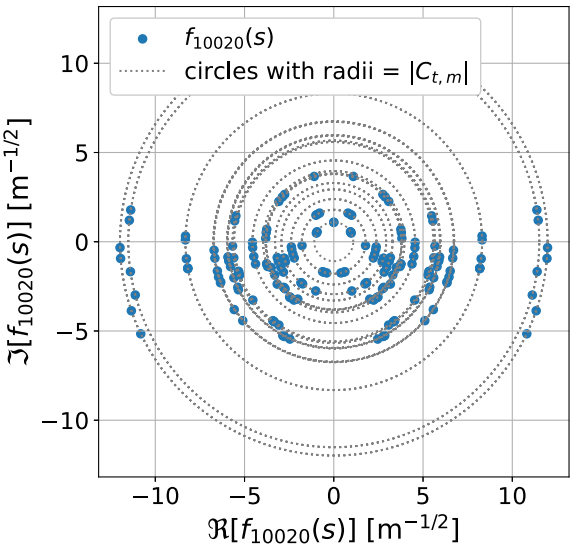

FIG. 3. Fluctuation of $f_{10020}(s)$ of the SSRF lattice in the complex plane for one SP. The blue dots are $f_{10020}(s)$ calculated at the entrances and exits of magnets.

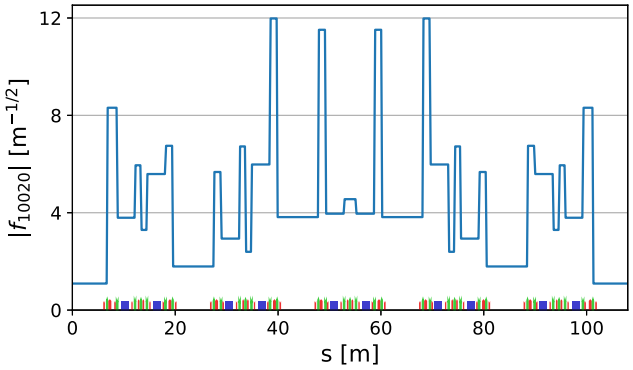

FIG. 4. The variation of the amplitude of the third-order RDT f_{10020} in one SP of the SSRF lattice.

amplitudes of the $e^{iu\boldsymbol{m}\cdot\boldsymbol{\mu}}$ terms of the RDT build-up fluctuation, i.e., $|C_{t,\boldsymbol{m}}|$. Note that the calculation of $|C_{t,\boldsymbol{m}}|$ for the fourth-order RDT fluctuations is different from the third-order case. So minimizing $|C_{t,\boldsymbol{m}}|$ is also helpful for controlling the two kinds of fourth-order RDT fluctuations.

Therefore, in this paper we use $h_{jklm0,\mathrm{ave}} = \sum_{t=1}^{N_1} |C_{t,\boldsymbol{m}}|/N_1$ to represent the fluctuation of one RDT, which is the average amplitude of $f_{jklm0}(s)$ at nonlinear magnets. Also, the effectiveness of controlling the average amplitude of the RDT build-up fluctuations is presented in Appendix B and compared with the average amplitude of $f_{jklm0}(s)$. Different RDTs driving different nonlinear effects are not of the same importance. It will be complicated to consider individual weights for different RDTs. For simplicity, in this paper, the RDTs of the same order have the same weight. The fluctuation of the nth order RDTs, denoted as $h_{n,\mathrm{ave}}$, is calculated as

$$h_{n,\mathrm{ave}} = \sqrt{\sum_{j+k+l+m=n} (h_{jklm0,\mathrm{ave}})^2}. \tag{7}$$

And we use $h_{n,\mathrm{ring}}$ to represent the nth order one-turn RDTs, which is defined in the same way as in Eq. (7). When the third- and fourth-order RDTs are considered simultaneously, we introduce a weight coefficient w for the fourth-order RDTs. For example, the sum of the third- and fourth-RDT fluctuations is calculated as $h_{3,\mathrm{ave}} + w \cdot h_{4,\mathrm{ave}}$. Besides, the ADTS terms also affect the on-momentum DA. We denote the one-turn ADTS terms as h_{ADTS}, which is calculated as

$$h_{\mathrm{ADTS}} = \sqrt{\left(\frac{d\nu_x}{dJ_x}\right)^2 + \left(\frac{d\nu_x}{dJ_y}\right)^2 + \left(\frac{d\nu_y}{dJ_y}\right)^2}. \tag{8}$$

By the way, calculating the RDT fluctuations is a necessary step to calculate the one-turn RDTs, which requires almost no additional calculations. With the data of third-order RDT fluctuations stored in the calculation,

we can directly have the values of $\sum_{a=1}^{b-1} \hat{V}_a$ in Eq. (4), allowing us to calculate the crossing terms using only one loop.

III. OPTIMIZATION OF A DBA LATTICE

Now we first use the SSRF lattice to analyze the nonlinear dynamics based on RDTs and their fluctuations. SSRF is a third-generation synchrotron light source with a beam energy of 3.5 GeV and a natural emittance of 3.9 nm · rad [21]. Its storage ring consists of four SPs with 20 DBA cells. Each SP has three standard cells and two matching cells. The linear optical functions and magnet layout of a half SP are shown in Fig. 5. There are two chromatic sextupole families (SD and SF) in the high dispersion regions, and 6 harmonic sextupole families (S1–S6) in the relatively low dispersion regions. The families S1, S3, and S5 are horizontally focusing sextupoles, and S2, S4, and S6 are defocusing ones.

In our nonlinear optimization, the strengths of six harmonic sextupole families are variables, with two chromatic sextupole families for fitting the corrected chromaticities to (1, 1). To statistically analyze the correlation between the RDTs and DA area, a large number of nonlinear solutions need to be generated. The probability of finding a nonlinear solution with a large DA in a randomly generated solution set is very small. Now that minimizing the RDTs of one-turn map is a necessary condition for enlarging the DA, we can increase the proportion of nonlinear solutions with large DAs by minimizing the RDTs. With a genetic algorithm toolbox geatpy [22], 10 000 nonlinear solutions were obtained after 40 generations of minimizing the third-order RDTs, and the third-order RDTs of some solutions are almost completely canceled. Then the on-momentum DA areas of all nonlinear solutions were calculated with ELEGANT [18].

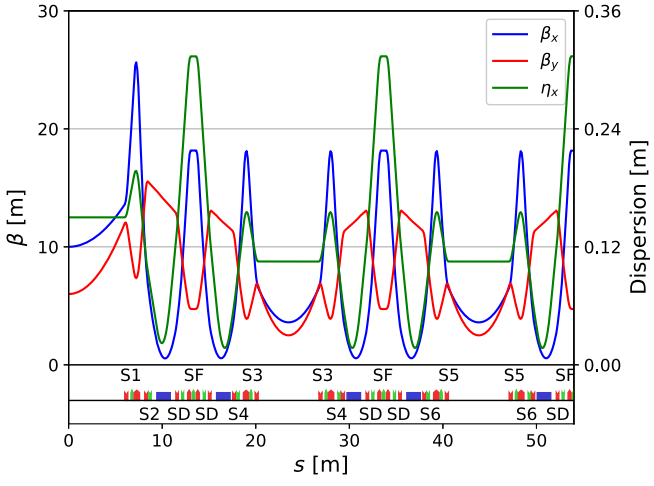

FIG. 5. Linear optical functions and magnet layout of a half SP of the SSRF lattice. In the layout, bends are in blue, quadrupoles in red, and sextupoles in green.

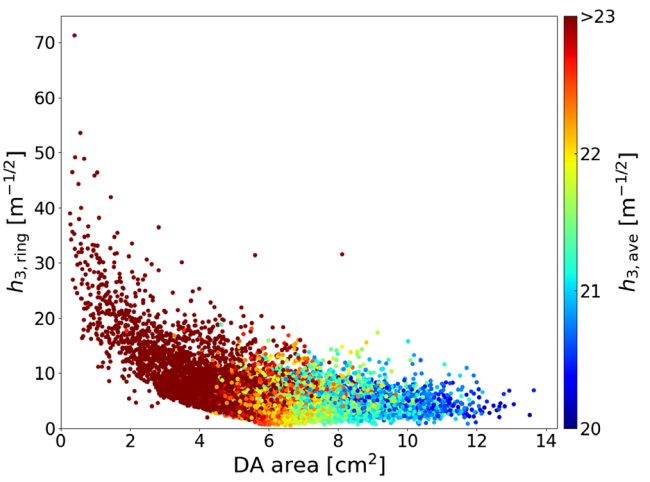

FIG. 6. Correlation between the DA area, the third-order one-turn RDTs $h_{3,\mathrm{ring}}$ and the third-order RDT fluctuations $h_{3,\mathrm{ave}}$ for the nonlinear solutions of the SSRF DBA lattice. Red color indicates large RDT fluctuations, and blue color indicates small RDT fluctuations.

Following Ref. [2], we show the correlation between the DA area and the third-order RDTs of one-turn map, i.e., $h_{3,\mathrm{ring}}$, for these solutions in Fig. 6. Besides, their RDT fluctuations $h_{3,\mathrm{ave}}$ are shown in the figure as a color bar. The correlation between DA area and $h_{3,\mathrm{ring}}$ roughly follows what was found in Ref. [2]: small $h_{3,\mathrm{ring}}$ is a necessary but not sufficient condition for large DA. However, the DA area has a stronger correlation with $h_{3,\mathrm{ave}}$. For a solution with small $h_{3,\mathrm{ave}}$, the probability of having a large DA area is larger than the solution with small $h_{3,\mathrm{ring}}$. Therefore, minimizing the RDT fluctuations is more effective than minimizing one-turn RDTs in enlarging the DA. Besides, there is an interesting thing that for the solutions with small $h_{3,\mathrm{ave}}$, their $h_{3,\mathrm{ring}}$ are not large.

The third-order RDTs are the most important in this DBA lattice [23]. For a more comprehensive comparison and a better understanding, the ADTS terms as well as the fourth-order RDTs were further involved in the nonlinear analysis. Of the generated solutions, the solutions with $h_{\mathrm{ADTS}} < 10\,000$ m^{-1} were used for the further analysis. For these solutions, Fig. 7 shows different correlations between the DA area, the one-turn RDTs and the fluctuations of RDTs. Figure 7(a) is another representation of Fig. 6, with the two axes representing $h_{3,\mathrm{ring}}$ and $h_{3,\mathrm{ave}}$ and the color bar representing DA area. It can be clearly seen that the colors are roughly layered horizontally, with solutions having large DAs, indicated by the red color, sinking to the bottom. In Appendix B, we make a similar figure with y axis representing the average amplitude of the RDT build-up fluctuations, indicating that controlling the RDT build-up fluctuations is also effective. In Fig. 7(b), the fourth-order RDTs are further involved with the weight coefficient $w = 0.01$ m$^{1/2}$. The RDT fluctuations are still pronounced,

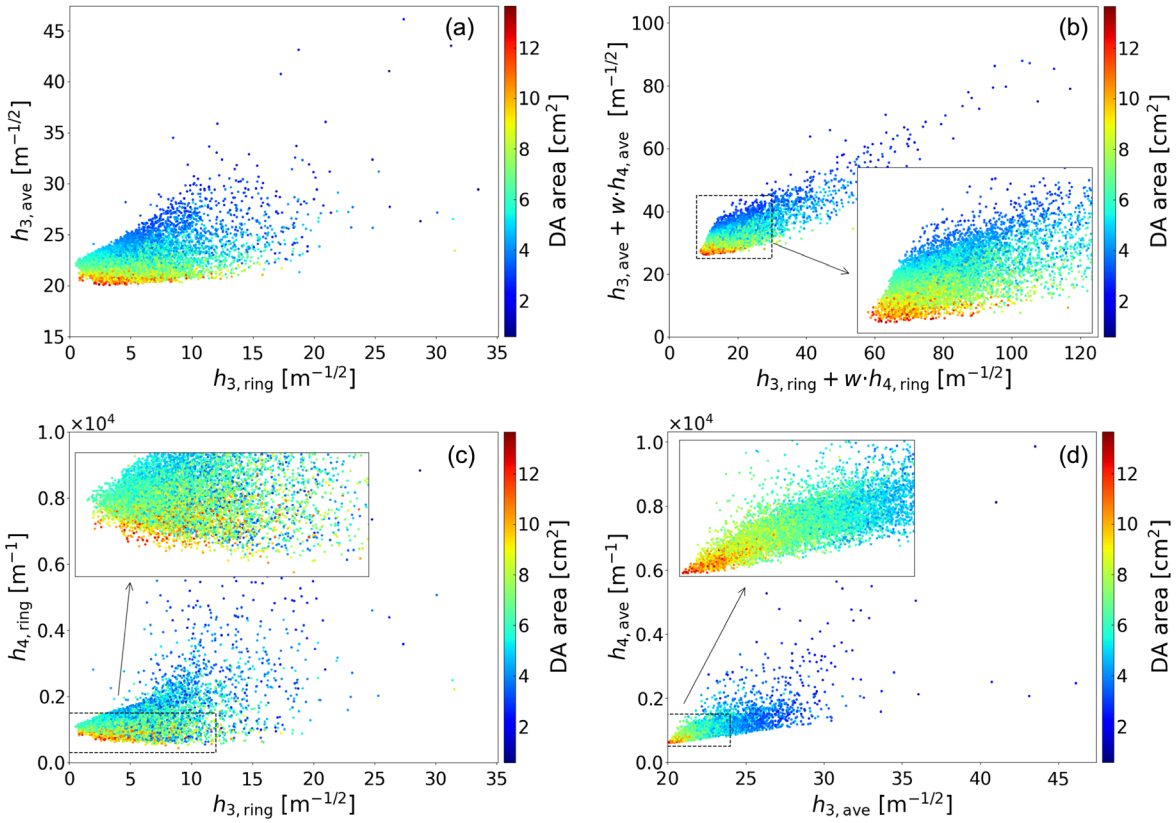

FIG. 7. Different correlations between the DA area, the third- and fourth-order RDTs of one-turn map and the fluctuations of these RDTs for the SSRF DBA lattice. Red color indicates large DA areas, and blue for small DA areas. The nonlinear solutions shown here have $h_{\mathrm{ADTS}} < 10\,000$ m^{-1}.

with colors again roughly layered. In the two lower plots, we step further to analyze the one-turn RDTs and the RDT fluctuations separately. Figure 7(c) shows the correlation between the third- and fourth-order one-turn RDTs and DA area. We can see that the colors are layered clearly only when $h_{3,\mathrm{ring}}$ is quite small. But when $h_{3,\mathrm{ring}}$ is relatively larger, many solutions with large differences in DA area are mixed together. This is because the third-order RDTs dominate in this DBA lattice, and the significance of $h_{4,\mathrm{ring}}$ emerges when $h_{3,\mathrm{ring}}$ is small. Comparing Figs. 7(a) and 7(c), we can find that minimizing $h_{3,\mathrm{ave}}$ is even more effective than minimizing the fourth-order term $h_{4,\mathrm{ring}}$. A possible explanation is that the crossing terms of lower-order RDTs generate higher-order RDTs, thus indicating a underlying connection between the higher-order RDTs and the fluctuation of lower-order RDTs. We will further demonstrate it in the next paragraph. In Fig. 7(d), the two axes are changed to $h_{3,\mathrm{ave}}$ and $h_{4,\mathrm{ave}}$. We can see that from the upper right to the lower left, the DA areas of these solutions gradually increase, and that the solutions with large DAs are on the tip of the lower left corner. This reflects that there is a strong positive correlation between the third-order and fourth-order RDT fluctuations in this lattice.

Figure 8 shows the correlation between the higher-order $h_{4,\mathrm{ring}}$, $h_{4,\mathrm{ave}}$ and the lower-order $h_{3,\mathrm{ave}}$. It is clear that both $h_{4,\mathrm{ring}}$ and $h_{4,\mathrm{ave}}$ roughly reduce as $h_{3,\mathrm{ave}}$ reduces. This verifies that controlling the fluctuation of the third-order

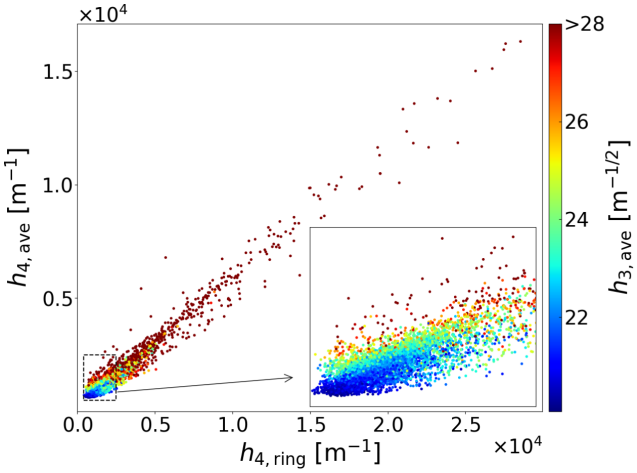

FIG. 8. Correlation between $h_{3,\mathrm{ave}}$, $h_{4,\mathrm{ring}}$, and $h_{4,\mathrm{ave}}$ for the SSRF DBA lattice. Red color indicates large $h_{3,\mathrm{ave}}$, and blue color for small $h_{3,\mathrm{ave}}$.

TABLE I. Nonlinear term values of two nonlinear solutions with similar RDT $h_{3,\mathrm{ring}}$, $h_{4,\mathrm{ring}}$ and ADTS terms but different RDT fluctuations $h_{3,\mathrm{ave}}$ and $h_{4,\mathrm{ave}}$.

	Smaller DA	Larger DA
$h_{3,\mathrm{ring}}$ ($\mathrm{m}^{-\frac{1}{2}}$)	3.5	3.6
$h_{4,\mathrm{ring}}$ (m^{-1})	901	897
$d\nu_x/dJ_x$ (m^{-1})	−315	−737
$d\nu_x/dJ_y$ (m^{-1})	857	1171
$d\nu_y/dJ_y$ (m^{-1})	−2082	−2472
$h_{3,\mathrm{ave}}$ ($\mathrm{m}^{-\frac{1}{2}}$)	23.2	20.7
$h_{4,\mathrm{ave}}$ (m^{-1})	961	693

RDTs is beneficial for controlling the fourth-order one-turn RDTs and the fourth-order RDT fluctuations due to the cross-talk effect. This is also consistent with Fig. 7(d). Furthermore, the cross-terms can generate even higher-order RDTs, such as fifth-order RDTs. As higher-order RDT fluctuations are reduced, even higher-order RDTs can also be controlled. This could be the underlying physics behind the strong correlation between reducing the RDT fluctuations and enlarging the DA. Higher-order RDTs are not only numerous in quantity, but also complicated to compute. It is cumbersome to directly reduce them, especially for fifth- and even higher-order RDTs. Therefore, we can minimize the fluctuations of lower-order RDTs to control them without calculating them.

We pick out two nonlinear solutions with approximately the same values of $h_{3,\mathrm{ring}}$, $h_{4,\mathrm{ring}}$ and ADTS terms, but their $h_{3,\mathrm{ave}}$ and $h_{4,\mathrm{ave}}$ are different. Table I shows these values of the two solutions. Their DAs with frequency map analysis [24] are tracked with ELEGANT and shown in Fig. 9. The one-turn RDTs and the RDT fluctuations are also shown in the figure. We can clearly see that the solution with smaller RDT fluctuations, i.e., smaller $h_{3,\mathrm{ave}}$ and $h_{4,\mathrm{ave}}$, has a larger DA. For the solution with smaller DA, the fifth-order resonance line $3\nu_x - 2\nu_y$ has a more significant effect. This verifies that controlling the fluctuations of third- and fourth-order RDTs is beneficial for controlling the fifth-order RDTs.

IV. OPTIMIZATION OF 6BA LATTICES

To achieve a diffraction-limited emittance with a reasonable circumference, MBA lattices are used in the design of DLSRs to replace DBA lattices [25,26]. In this section, we will use DLSR MBA lattices to study the correlation between RDT fluctuations and DA area again. In these lattices with strong focusing, the nonlinear effects become strong. HOA is a successful approach to control the nonlinear effects and has been used in some DLSR lattice designs [9,27–31]. In an HOA MBA lattice with appropriate bend unit cell tunes, most or all of the third- and fourth-order geometric RDTs can be canceled over some identical cells [32]. Here the MBA lattices used are two HOA 6BA lattices that we designed in Refs. [29,33], which have five identical unit cells, each with horizontal and vertical tunes of (0.4, 0.1). In this kind of HOA lattices, the fourth-order RDT h_{20200} cannot be canceled in the ideal cancellation condition [32]. Besides, in these 6BA lattices, the HOA approach was also used for further nonlinear cancellation over some lattice cells. For one of the 6BA lattices, the term h_{20200} is still not canceled over some lattice cells; while for the other one, h_{20200} is canceled over lattice cells.

A. The first 6BA lattice

The first 6BA lattice we will study was designed in Ref. [33]. The designed storage ring is a 2.2 GeV DLSR with a natural emittance of 94 pm · rad, which consists of 16 identical lattice cells. The optical functions of this lattice are shown in Fig. 10. The horizontal and vertical tunes of a lattice cell are close to $(2 + 5/8, 7/8)$, enabling nonlinear cancellation over eight cells. However, neither the lattice cell tunes nor the unit cell tunes are able to cancel h_{20200}. To further optimize the nonlinear dynamics, including the control of ADTS terms, the sextupoles are symmetrically grouped into eight families as illustrated in Fig. 10, and a family of octupoles is used as in Ref. [33].

Similar to the DBA lattice, we use genetic algorithm to increase the proportion of solutions with good dynamic performance for better nonlinear analysis. But here three objectives $h_{3,\mathrm{ring}}$, $h_{4,\mathrm{ring}}$, and h_{ADTS} were optimized simultaneously, since fourth-order RDTs and ADTS terms become more important in the nonlinear optimization of DLSR lattices. The chromaticities were corrected to (2,2). The genetic algorithm ran 10 generations with a population size of 10 000. The fourth-order RDT build-up fluctuations of one optimized solution along the ring are shown in Fig. 11. The term h_{20200} exhibits a significant rise in magnitude along the ring, while the other terms are well suppressed. As previously mentioned, the term h_{20200} cannot be canceled in two HOA schemes, i.e., nonlinear cancellation within a single lattice cell and over eight lattice cells, and can only be controlled through the nonlinear optimization with sextupole grouping.

For the optimized solutions, their $h_{3,\mathrm{ave}}$, $h_{4,\mathrm{ave}}$, and DA areas were calculated. Figure 12 shows the correlation between the RDT fluctuations, ADTS terms, and DA area. The weight coefficient w is also set to 0.01 m^{-1} in this lattice. Compared to the DBA lattice, ADTS terms are more difficult to control in this 6BA lattice with stronger focusing. Most of the solutions with large ADTS values have small DA areas. For the solutions with both small ADTS values and small RDT fluctuations, most of them have large DAs. We use the solutions with $h_{\mathrm{ADTS}} < 1 \times 10^5$ m^{-1} for further analysis. The correlation between RDT fluctuations and one-turn RDTs is shown in the upper plot of Fig. 13. We can see that similar to the DBA lattice

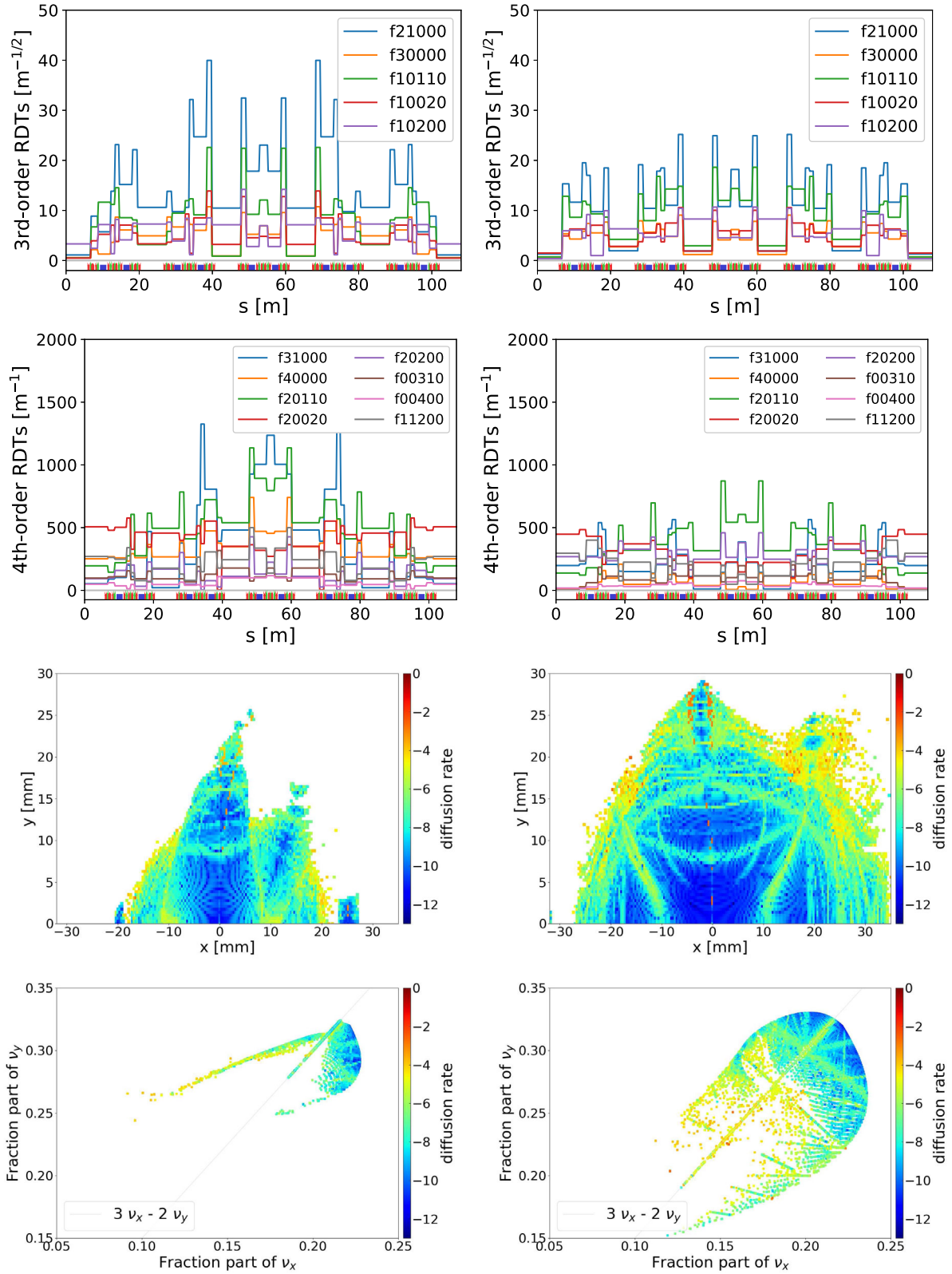

FIG. 9. Two nonlinear solutions of the SSRF DBA lattice with similar one-turn RDT and ADTS terms but different RDT fluctuations and DA areas. The left four plots are for one solution, and the right four for the other solution. The upper four plots show the third- and fourth-order RDT fluctuations, and the lower four plots are the frequency map analysis of DAs. The values of these nonlinear terms are listed in Table I.

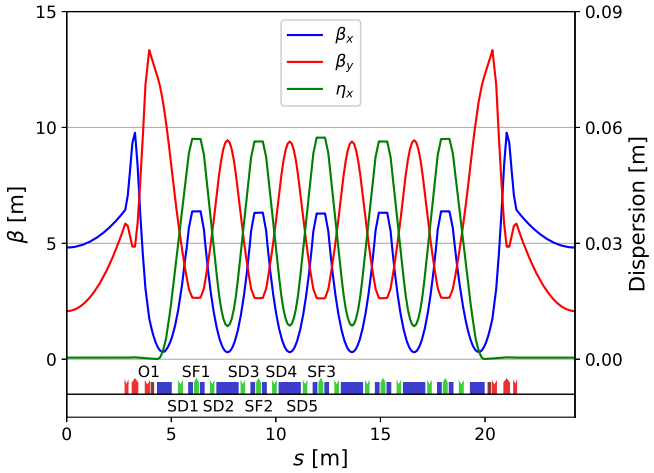

FIG. 10. Linear optical functions and magnet layout of one cell of the first 6BA lattice. In the layout, bends are in blue, quadrupoles in red, sextupoles in green, and octupoles in brown.

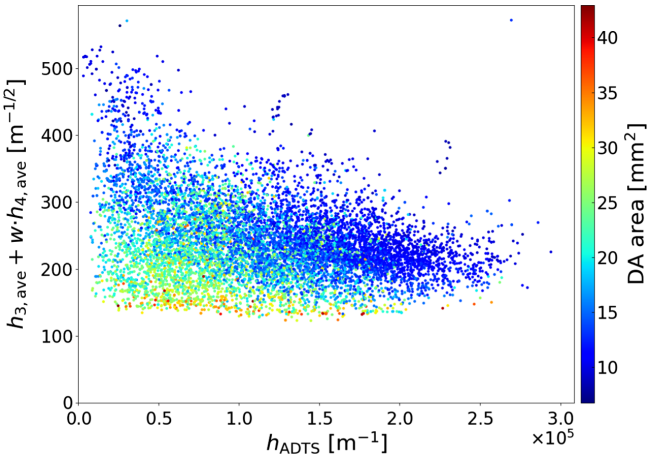

FIG. 12. Correlation between the ADTS terms, the RDT fluctuations and the DA areas for the first 6BA lattice.

case, DA area has a stronger correlation with RDT fluctuations than one-turn RDTs, with the red color sinking to the bottom. Besides, the differences in RDT fluctuations of these solutions can be large when their one-turn RDTs are controlled. The lower plot of Fig. 13 shows that the term $h_{20200,\mathrm{ave}}$ contributes the main difference. We can see that for the solutions with small $h_{20200,\mathrm{ave}}$, most of them have large DA areas. And for the solutions with small $h_{20200,\mathrm{ave}}$ but large fluctuations of other RDTs, their DAs are small, indicating that controlling the fluctuation of other RDTs is also important.

B. The second 6BA lattice

The second 6BA lattice to be studied was designed in Ref. [29]. The beam energy is also 2.2 GeV. But the storage

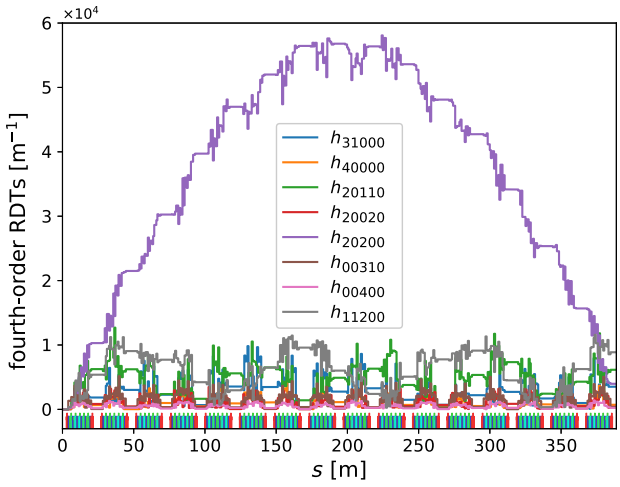

FIG. 11. The fourth-order RDT build-up fluctuations along the first 6BA ring of a nonlinear solution. The RDT h_{20200} rises very high.

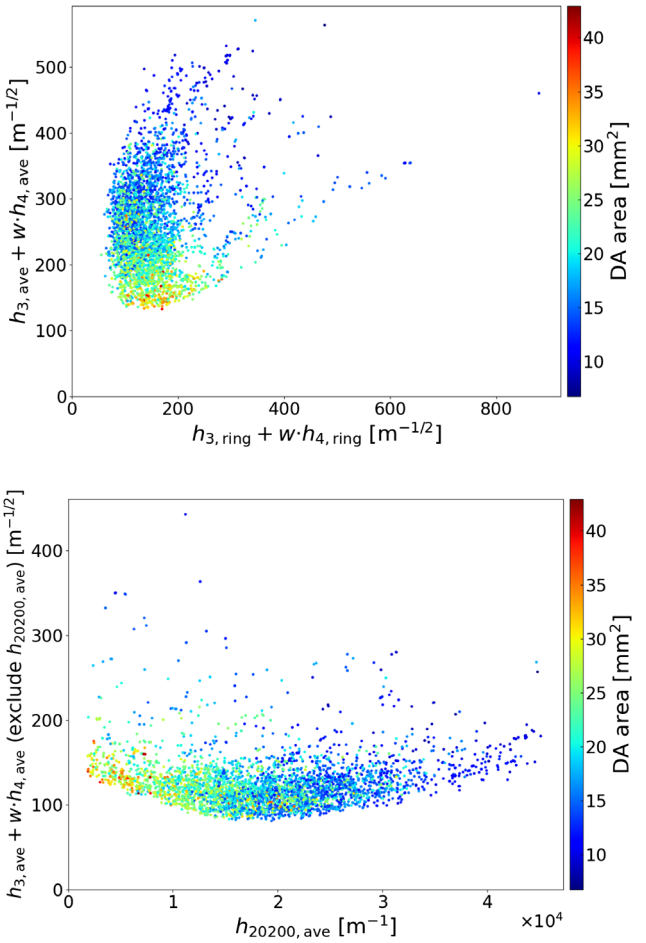

FIG. 13. Upper plot: correlation between the DA area, the one-turn RDTs, and the RDT fluctuations for the first 6BA. Lower plot: correlation between the DA area, the fluctuation of h_{20200}, and other RDT fluctuations. The nonlinear solutions shown here have $h_{\mathrm{ADTS}} < 1 \times 10^5$ m^{-1}.

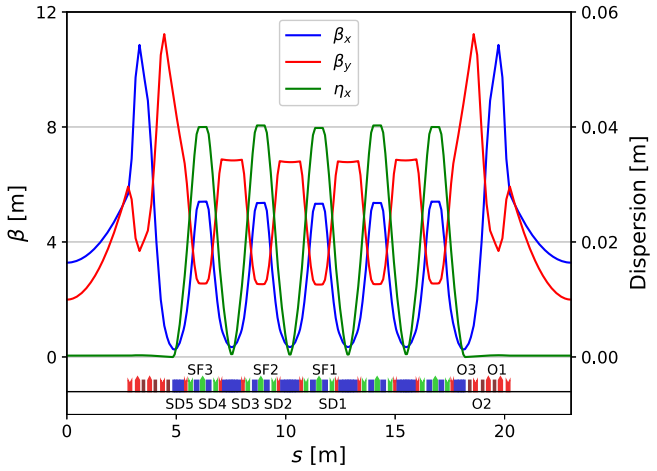

FIG. 14. Linear optical functions and magnet layout of the second 6BA lattice cell.

ring consists of 20 identical lattice cells and has a lower natural emittance of 36 pm rad and lower beta functions in straight sections. Figure 14 shows one cell of this lattice. Different from the first 6BA lattice, the horizontal and vertical tunes of this lattice cell are approximately (2.7,0.9) to make the nonlinear cancellation over 10 cells, including the cancellation of h_{20200}. In this lattice, the sextupoles are also symmetrically grouped as shown in Fig. 14. There are eight families of chromatic sextupoles and three families of harmonic octupoles used for the nonlinear optimization, with the chromaticities corrected to $(-3,-3)$ due to negative momentum compaction factor.

For the nonlinear analysis, the three objectives $h_{3,\mathrm{ring}}$, $h_{4,\mathrm{ring}}$ and h_{ADTS} were also optimized with a population of 10 000 and 20 generations here. The correlation between the RDT fluctuations, ADTS terms and DA area is shown in Fig. 15. The weight coefficient $w = 0.01$ m^{-1}. Compared to the first 6BA lattice, this lattice has stronger

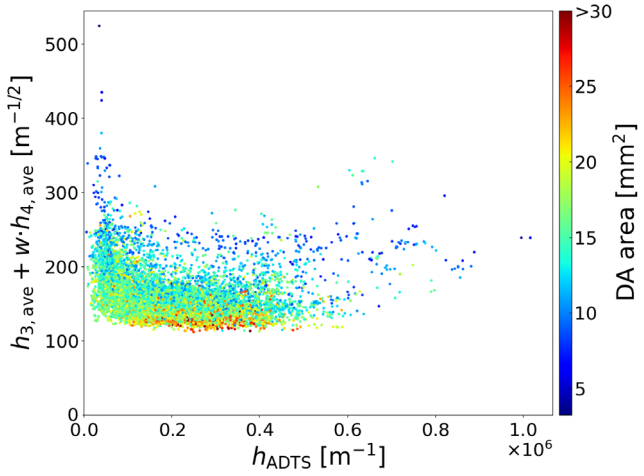

FIG. 15. Correlation between the ADTS terms, the RDT fluctuations and the DA areas for the second 6BA lattice.

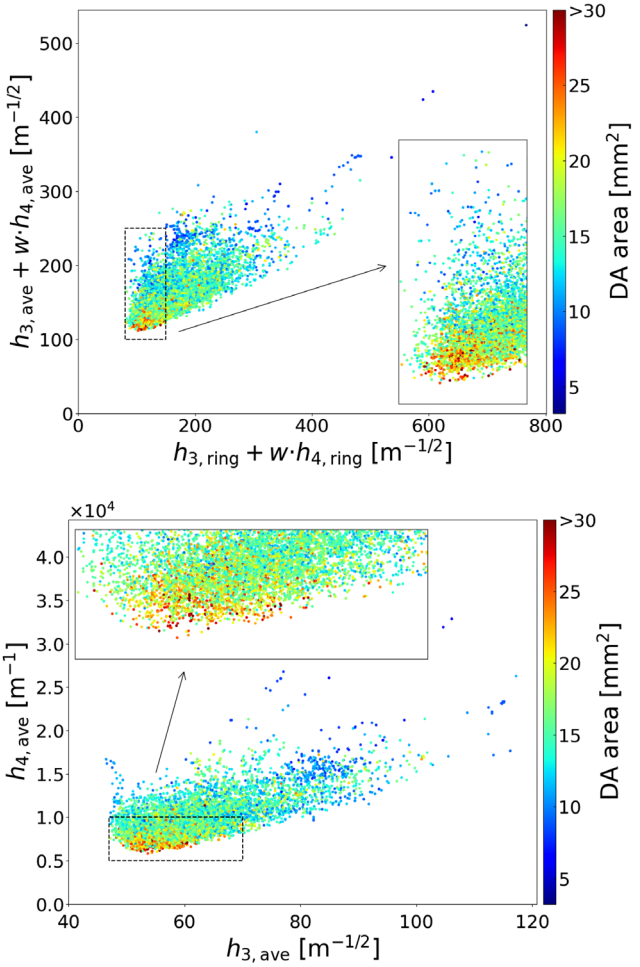

FIG. 16. Upper plot: correlation between the DA area, the one-turn RDTs and the RDT fluctuations for the second 6BA. Lower plot: correlation between the DA area, the third- and fourth-order RDT fluctuations with different orders being considered separately. The nonlinear solutions shown here have $h_{\mathrm{ADTS}} < 5 \times 10^5$ m^{-1}.

nonlinear effects with larger ADTS terms. Nonetheless, possibly due to the effective suppression of resonances with the HOA strategy, even if the ADTS terms are large, there are still some solutions with large DAs. Next we analyze the solutions with $h_{\mathrm{ADTS}} < 5 \times 10^5$ m^{-1}. The upper plot of Fig. 16 shows the correlation between one-turn RDTs, RDT fluctuations, and DA area. Compared to the first 6BA, here the range of $h_{3,\mathrm{ave}} + w \cdot h_{4,\mathrm{ave}}$ of the solutions is smaller when one-turn RDTs are controlled. This is because h_{20200} is prevented from building up in this lattice. And we can see that the solutions with large DAs are mainly at the bottom, indicating the effectiveness of minimizing RDT fluctuations. In the lower plot, just like Fig. 7(d), we further analyze the third- and fourth-order RDT fluctuations separately. Most solutions with large DAs have small $h_{3,\mathrm{ave}}$ and $h_{4,\mathrm{ave}}$, which is consistent with Fig. 7(d). But different from Fig. 7(d), there are also some

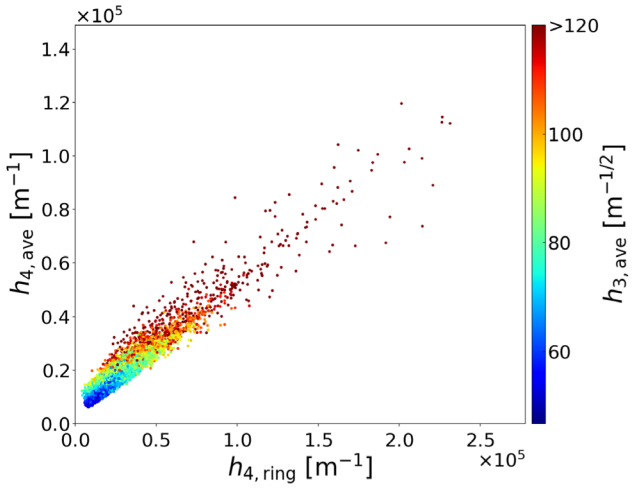

FIG. 17. Correlation between $h_{3,\mathrm{ave}}$, $h_{4,\mathrm{ring}}$, and $h_{4,\mathrm{ave}}$ for the second 6BA lattice.

solutions with small $h_{3,\mathrm{ave}}$ and $h_{4,\mathrm{ave}}$ have small DAs. This needs to be further studied. We have preliminarily found that optimizing the weight of each RDT can strengthen the correlation between RDT fluctuations and DA area, since different resonances have different effects on DA.

We have shown that reducing the lower-order RDT fluctuations is beneficial for controlling higher-order RDTs in the DBA lattice. But in this 6BA lattice, the fourth-order RDT fluctuations are contributed not only by the crossing terms of sextupoles, but also by the octupoles, and $h_{3,\mathrm{ave}}$ only affects the former. To verify the correlation between third-order RDT fluctuations and fourth-order RDTs in this lattice like in Fig. 8, we generated another set of nonlinear solutions by optimizing $h_{3,\mathrm{ave}}$ for some generations, where the octupoles were not employed. For these solutions, the ones with smaller $h_{3,\mathrm{ave}}$ also have smaller $h_{4,\mathrm{ave}}$ and $h_{4,\mathrm{ring}}$, as shown in Fig. 17. This is consistent with Fig. 8. In the lower plot of Fig. 16, the correlation between $h_{3,\mathrm{ave}}$ and $h_{4,\mathrm{ave}}$ is weaker than that in Fig. 17 due to that the octupoles also contribute to fourth-order RDTs.

V. CONCLUSION AND OUTLOOK

Inspired by the fact that the local cancellation of nonlinear dynamics effects adopted in some DLSR lattices is more effective than the global cancellation, we studied the analysis of nonlinear dynamics based on minimizing the RDT fluctuations. Physical analysis showed that the RDT fluctuations are involved in the calculation of crossing terms. Minimizing the RDT fluctuations is beneficial for controlling the crossing terms and thus enlarging the DA. A DBA lattice and two 6BA lattices were taken as examples for this study. It was found that reducing the RDT fluctuations has a very strong correlation with enlarging the DA area. Nonlinear solutions with small RDT fluctuations are much more likely to have large DAs than those with small one-turn RDTs. And for the solutions with small RDT fluctuations, their one-turn RDTs are also controlled. Moreover, reducing lower-order RDT fluctuations can also reduce higher-order one-turn RDTs and higher-order RDT fluctuations. The higher-order RDTs contributed by the crossing terms of lower-order RDTs are not only numerous but also computationally complicated, especially for the fifth-order and higher-order RDTs. The fifth-order case was demonstrated in the DBA lattice. The effectiveness of controlling RDT fluctuations in enlarging DA confirms once again that the local nonlinear cancellation is more effective than the global cancellation. Note that the nonlinear analysis based on minimizing the RDT fluctuations is in the framework of minimizing RDTs, but using minimizing the average RDTs instead of minimizing the commonly-used one-turn RDTs. This means that minimizing the RDT fluctuations is still not a sufficient condition for enlarging the DA, but it is more effective than minimizing one-turn RDTs.

The average amplitude of $f_{jklm0}(s)$ was used to quantitatively represent the RDT fluctuation in this paper, and the average amplitude of the RDT build-up fluctuation is also effective as presented in Appendix B. For the codes having the function of calculating the variation of RDTs along the longitudinal position, i.e., the RDT fluctuations, such as ELEGANT [18] and AT [34], it is easy to further include the calculation of the quantity representing the RDT fluctuation as used in this paper. So the analysis and optimization of DA based on controlling the fluctuation of RDTs can also be implemented with these codes.

Since reducing the RDT fluctuations can enlarge the DA area more effectively than reducing the one-turn RDTs, we can consider minimizing RDT fluctuations in the DA optimization. By using evolutionary algorithms, we can first minimize RDT fluctuations to effectively and quickly find the regions where large DA solutions exist, and then in these regions, DA can be further optimized based on particle tracking. Although this paper focused on on-momentum DA and the fluctuation of geometric RDTs, it is possible that the fluctuation of chromatic terms related to off-momentum dynamics can be further considered in the nonlinear optimization. In addition, the RDT fluctuations can provide physical feedback for adjusting linear optics to achieve better nonlinear dynamics performance.

The quality of DA is related to both the area of the DA and the diffusion rate inside the DA. Lower diffusion rates indicate that the motion of particles is more regular [24] and the DA has better robustness against errors. Since reducing RDT fluctuations can control both lower-order and higher-order resonances, it may lead to lower diffusion rates. Therefore, we will further study the correlation between RDT fluctuations, DA area and diffusion rates using frequency map analysis. Besides, machine learning, which has been successfully applied to the nonlinear dynamics

optimization in recent years [35–40], can also be used to enhance the study in this paper, including better characterization of the RDT fluctuations. Since reducing RDT fluctuations is more effective than reducing one-turn or one-period RDTs, we can explore new lattices based on minimizing the RDT fluctuations in the linear and nonlinear optimization of a general magnet layout.

ACKNOWLEDGMENTS

One of the authors (Z. B.) would like to thank Alexandre Loulergue, Laurent S. Nadolski, and Ryutaro Nagaoka of SOLEIL for helpful discussions. This work was supported by the National Natural Science Foundation of China under Grant No. 11875259 and the National Key Research and Development Program of China under Grant No. 2016YFA0402000.

APPENDIX A: FLUCTUATION OF THE FOURTH-ORDER RDTs

As in Sec. II, here we also use $\boldsymbol{m} = (j-k, l-m)$ to represent the mode of h_{jklm0}, which drives the resonance $(j-k)\nu_x + (l-m)\nu_y$. For simplicity, we substitute h_{jklm0} with $h_{\boldsymbol{m}}$. The fourth-order RDTs are contributed by octupoles and the crossing terms of sextupoles. The fluctuation of the fourth-order RDTs contributed by octupoles is as simple as the third-order RDTs in Sec. II [41], and with the number of lattice periods u as a variable, the fluctuation of such a RDT can be described by a constant term and the $e^{iu\boldsymbol{m}\cdot\boldsymbol{\mu}}$ term. In the following we will characterize the fluctuation of the fourth-order RDTs contributed by the crossing terms of sextupoles.

For a lattice period with N_1 sextupoles, we denote the period tunes as $\boldsymbol{\mu} = 2\pi(\nu_x, \nu_y)$ and the phase advances as $\boldsymbol{\phi} = (\phi_x, \phi_y)$. And we use $h_{t,\boldsymbol{m}}$ to represent the contribution of the tth sextupole to the third-order RDT. The sextupole terms $h_{a,\boldsymbol{m}_1}$ and $h_{b,\boldsymbol{m}_2}$ drive the fourth-order resonance $\boldsymbol{m} = \boldsymbol{m}_1 + \boldsymbol{m}_2$ by the cross-talk effect [7]:

$$\frac{1}{2}\sum_{b>a=1}^{N_1}\Big[h_{a,\boldsymbol{m}_1}(2J_x)^{\frac{j_1+k_1}{2}}(2J_y)^{\frac{l_1+m_1}{2}}e^{i\boldsymbol{m}_1\boldsymbol{\phi}}, h_{b,\boldsymbol{m}_2}(2J_x)^{\frac{j_2+k_2}{2}}(2J_y)^{\frac{l_2+m_2}{2}}e^{i\boldsymbol{m}_2\boldsymbol{\phi}}\Big]. \tag{A1}$$

We move the terms $h_{a,\boldsymbol{m}_1}$ and $h_{b,\boldsymbol{m}_2}$ outside the Poisson bracket, then the coefficient of the Poisson bracket is $\frac{1}{2}\sum_{b>a=1}^{N_1} h_{a,\boldsymbol{m}_1}h_{b,\boldsymbol{m}_2}$.

The crossing term fluctuation arises from the change of $\sum_{b>a=1}^{t} h_{a,\boldsymbol{m}_1}h_{b,\boldsymbol{m}_2}$ with t. For multiple lattice periods, at the $(u+1)$th period ($u \geq 0$),

$$\begin{aligned}&\sum_{b>a=1}^{u\cdot N_1+t} h_{a,\boldsymbol{m}_1}h_{b,\boldsymbol{m}_2}\\ &= \sum_{b=2}^{u\cdot N_1+t}\sum_{a=1}^{b-1} h_{a,\boldsymbol{m}_1}h_{b,\boldsymbol{m}_2}\\ &= \sum_{b=2}^{u\cdot N_1}\sum_{a=1}^{b-1} h_{a,\boldsymbol{m}_1}h_{b,\boldsymbol{m}_2} + \sum_{b=u\cdot N_1+1}^{u\cdot N_1+t}\sum_{a=1}^{b-1} h_{a,\boldsymbol{m}_1}h_{b,\boldsymbol{m}_2}.\end{aligned} \tag{A2}$$

We denote that $h_{a,\boldsymbol{m}_1}$ is at the (u_a+1)th period and $h_{b,\boldsymbol{m}_2}$ is at the (u_b+1)th period, with $u_b \geq u_a \geq 0$. The first part in Eq. (A2) can be divided into two parts with $u_b = u_a$ and $u_b > u_a$. Then we have

$$\begin{aligned}\sum_{b=2}^{u\cdot N_1}\sum_{a=1}^{b-1} h_{a,\boldsymbol{m}_1}h_{b,\boldsymbol{m}_2} &= \sum_{u_a=0}^{u-1}\sum_{b>a=1}^{N_1} h_{(u_a\cdot N_1+a),\boldsymbol{m}_1}h_{(u_a\cdot N_1+b),\boldsymbol{m}_2} + \sum_{u_b>u_a=0}^{u-1}\sum_{a,b=1}^{N_1} h_{(u_a\cdot N_1+a),\boldsymbol{m}_1}h_{(u_b\cdot N_1+b),\boldsymbol{m}_2}\\ &= \sum_{u_a=0}^{u-1}\sum_{b>a=1}^{N_1} h_{a,\boldsymbol{m}_1}h_{b,\boldsymbol{m}_2}e^{iu_a(\boldsymbol{m}_1+\boldsymbol{m}_2)\cdot\boldsymbol{\mu}} + \sum_{u_b>u_a=0}^{u-1}\sum_{a,b=1}^{N_1} h_{a,\boldsymbol{m}_1}h_{b,\boldsymbol{m}_2}e^{i(u_a\boldsymbol{m}_1+u_b\boldsymbol{m}_2)\cdot\boldsymbol{\mu}}\\ &= \left(\sum_{b>a=1}^{N_1} h_{a,\boldsymbol{m}_1}h_{b,\boldsymbol{m}_2}\right)\frac{1-e^{iu(\boldsymbol{m}_1+\boldsymbol{m}_2)\cdot\boldsymbol{\mu}}}{1-e^{i(\boldsymbol{m}_1+\boldsymbol{m}_2)\cdot\boldsymbol{\mu}}} + \left(\sum_{a,b=1}^{N_1} h_{a,\boldsymbol{m}_1}h_{b,\boldsymbol{m}_2}\right)\sum_{u_b=1}^{u-1} e^{iu_b\boldsymbol{m}_2\cdot\boldsymbol{\mu}}\frac{1-e^{iu_b\boldsymbol{m}_1\cdot\boldsymbol{\mu}}}{1-e^{i\boldsymbol{m}_1\cdot\boldsymbol{\mu}}}\\ &= \left(\sum_{b>a=1}^{N_1} h_{a,\boldsymbol{m}_1}h_{b,\boldsymbol{m}_2}\right)\frac{1-e^{iu(\boldsymbol{m}_1+\boldsymbol{m}_2)\cdot\boldsymbol{\mu}}}{1-e^{i(\boldsymbol{m}_1+\boldsymbol{m}_2)\cdot\boldsymbol{\mu}}} + \frac{\sum_{a,b=1}^{N_1} h_{a,\boldsymbol{m}_1}h_{b,\boldsymbol{m}_2}}{1-e^{i\boldsymbol{m}_1\cdot\boldsymbol{\mu}}}\left(\frac{1-e^{iu\boldsymbol{m}_2\cdot\boldsymbol{\mu}}}{1-e^{i\boldsymbol{m}_2\cdot\boldsymbol{\mu}}} - \frac{1-e^{iu(\boldsymbol{m}_1+\boldsymbol{m}_2)\cdot\boldsymbol{\mu}}}{1-e^{i(\boldsymbol{m}_1+\boldsymbol{m}_2)\cdot\boldsymbol{\mu}}}\right),\end{aligned} \tag{A3}$$

where $h_{(u\cdot N_1+t),\boldsymbol{m}} = h_{t,\boldsymbol{m}}e^{iu\boldsymbol{m}\cdot\boldsymbol{\mu}}$. And the second part in Eq. (A2) is

$$\sum_{b=u\cdot N_1+1}^{u\cdot N_1+t}\sum_{a=1}^{b-1} h_{a,\boldsymbol{m}_1}h_{b,\boldsymbol{m}_2} = \sum_{b=u\cdot N_1+1}^{u\cdot N_1+t}\sum_{a=1}^{u\cdot N_1} h_{a,\boldsymbol{m}_1}h_{b,\boldsymbol{m}_2} + \sum_{b=u\cdot N_1+2}^{u\cdot N_1+t}\sum_{a=u\cdot N_1+1}^{b-1} h_{a,\boldsymbol{m}_1}h_{b,\boldsymbol{m}_2}$$
$$= \left(\sum_{a=1}^{N_1} h_{a,\boldsymbol{m}_1}\frac{1-e^{iu\boldsymbol{m}_1\cdot\boldsymbol{\mu}}}{1-e^{i\boldsymbol{m}_1\cdot\boldsymbol{\mu}}}\right)\left(\sum_{b=1}^{t} h_{b,\boldsymbol{m}_2}e^{iu\boldsymbol{m}_2\cdot\boldsymbol{\mu}}\right) + \sum_{b=2}^{t}\sum_{a=1}^{b-1} h_{a,\boldsymbol{m}_1}h_{b,\boldsymbol{m}_2}e^{iu(\boldsymbol{m}_1+\boldsymbol{m}_2)\cdot\boldsymbol{\mu}}$$
$$= \left(\sum_{a=1}^{N_1} h_{a,\boldsymbol{m}_1}\right)\left(\sum_{b=1}^{t} h_{b,\boldsymbol{m}_2}\right)\frac{e^{iu\boldsymbol{m}_2\cdot\boldsymbol{\mu}}-e^{iu(\boldsymbol{m}_1+\boldsymbol{m}_2)\cdot\boldsymbol{\mu}}}{1-e^{i\boldsymbol{m}_1\cdot\boldsymbol{\mu}}} + \left(\sum_{b>a=1}^{t} h_{a,\boldsymbol{m}_1}h_{b,\boldsymbol{m}_2}\right)e^{iu(\boldsymbol{m}_1+\boldsymbol{m}_2)\cdot\boldsymbol{\mu}}. \quad \text{(A4)}$$

With Eqs. (A3) and (A4), we can construct the fourth-order RDT build-up fluctuations of multiple periods based on the RDTs of one period. With the number of periods u as a variable, the crossing terms include the $e^{iu\boldsymbol{m}_2\cdot\boldsymbol{\mu}}$ term, the $e^{iu(\boldsymbol{m}_1+\boldsymbol{m}_2)\cdot\boldsymbol{\mu}}$ term and constant term. Note that the constant term is in Eq. (A3). According to Eq. (5), the coefficient of the $e^{iu\boldsymbol{m}_2\cdot\boldsymbol{\mu}}$ term in Eq. (A3) + Eq. (A4), i.e., $\frac{\sum_{a=1}^{N_1} h_{a,\boldsymbol{m}_1}}{1-e^{i\boldsymbol{m}_1\cdot\boldsymbol{\mu}}}\left(-\frac{\sum_{b=1}^{N_1} h_{b,\boldsymbol{m}_2}}{1-e^{i\boldsymbol{m}_2\cdot\boldsymbol{\mu}}}+\sum_{b=1}^{t} h_{b,\boldsymbol{m}_2}\right)$, is equal to $C_{0,\boldsymbol{m}_1}C_{t,\boldsymbol{m}_2}$, where $C_{0,\boldsymbol{m}_1}$ is the third-order one-period RDT and $C_{t,\boldsymbol{m}_2}$ indicates the third-order RDT fluctuation. And remember that $\sum_{b>a=1}^{t} h_{a,\boldsymbol{m}_2}h_{b,\boldsymbol{m}_1}$ also drives the same resonance $\boldsymbol{m}_1+\boldsymbol{m}_2$. So there is also the $e^{iu\boldsymbol{m}_1\cdot\boldsymbol{\mu}}$ term. Moreover, some fourth-order RDTs consist of more than one pair of crossing terms. For example, h_{20110} is contributed by $h_{30000}h_{01110}$, $h_{21000}h_{10110}$, and $h_{10200}h_{10020}$ [7], and there are more terms in its fluctuation.

Here we show an example of the h_{31000} build-up fluctuation of the second 6BA lattice. The RDT h_{31000} is contributed by h_{30000} and h_{12000} through cross-talk. Let $\boldsymbol{m}_1=(3,0)$, $\boldsymbol{m}_2=(-1,0)$, and $\boldsymbol{m}=\boldsymbol{m}_1+\boldsymbol{m}_2=(2,0)$. The values of $h_{1\to u\cdot N_1+t,31000}$ of the second 6BA, with u varying from 1 to 50, were calculated, and the results of $t=4$ and N_1 are shown in Fig. 18. The fourth-order RDT build-up fluctuation has the form of $C_{0,\boldsymbol{m}}+C_{t,\boldsymbol{m}}e^{iu\boldsymbol{m}\cdot\boldsymbol{\mu}}+C'_{t,\boldsymbol{m}_1}e^{iu\boldsymbol{m}_1\cdot\boldsymbol{\mu}}+C'_{t,\boldsymbol{m}_2}e^{iu\boldsymbol{m}_2\cdot\boldsymbol{\mu}}$, with $C_{0,\boldsymbol{m}}$, $C_{t,\boldsymbol{m}}$, $C'_{t,\boldsymbol{m}_1}$, and $C'_{t,\boldsymbol{m}_2}$ being four coefficients. Note that the

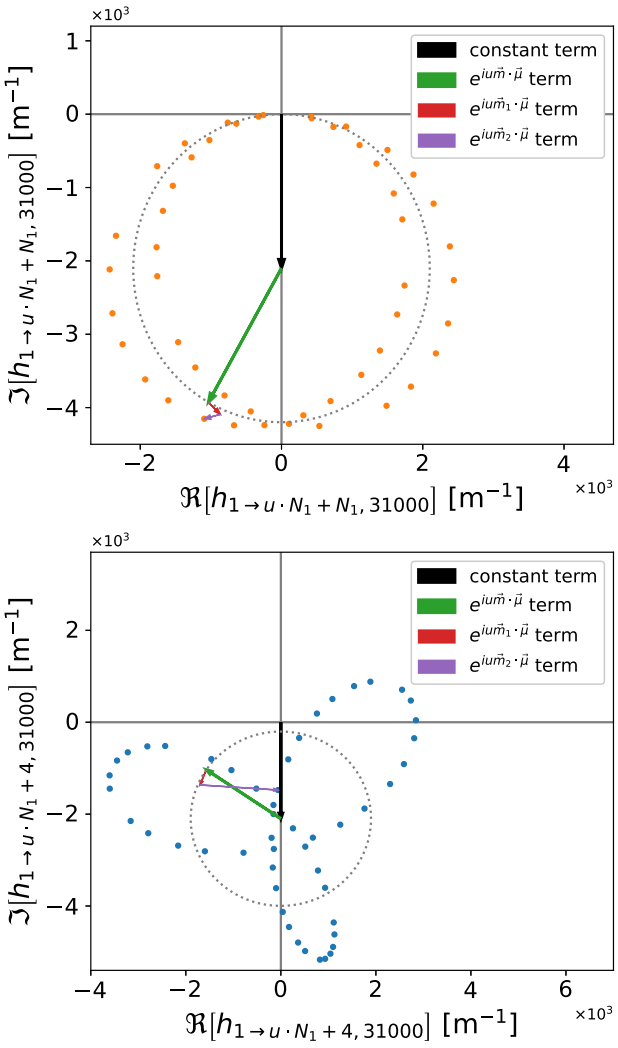

FIG. 18. The values of $h_{1\to u\cdot N_1+t,31000}$ of the second 6BA lattice contributed by four terms, with u varying from 1 to 50. The upper plot is the case with $t=N_1$, and the lower plot is the $t=4$ case.

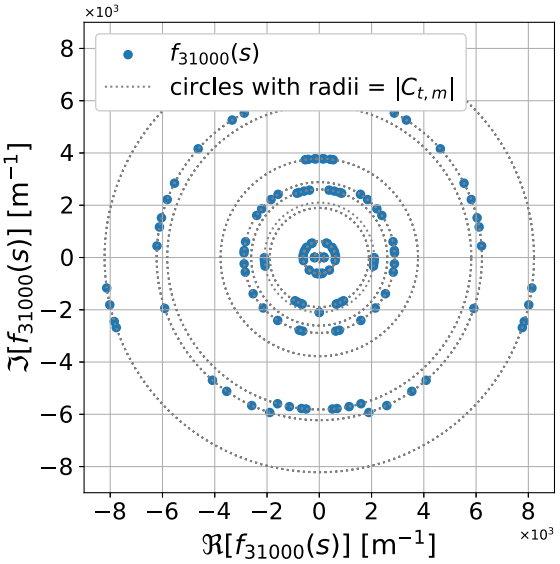

FIG. 19. Fluctuation of $f_{31000}(s)$ of the second 6BA lattice in the complex plane for one period. The blue dots are $f_{31000}(s)$ calculated at the entrances and exits of magnets.

expression of $C_{0,\boldsymbol{m}}$ and $C_{t,\boldsymbol{m}}$ here is different from the case of third-order RDTs shown in Eq. (5). For each sextupole index t, the fourth-order RDT build-up fluctuation is around the circle $C_{0,\boldsymbol{m}} + C_{t,\boldsymbol{m}} e^{i\boldsymbol{u}\boldsymbol{m}\cdot\boldsymbol{\mu}}$ as shown in Fig. 18, which is different from the third-order RDT case. The circle passes the origin in the complex plane when $t = N_1$. Reducing the third-order RDT fluctuations brings these dots closer to the dashed circles. Moreover, reducing the fourth-order RDT fluctuations leads to smaller radii of the circles. As for the second kind of RDT fluctuations, the calculation is referred to Ref. [17]. We found that the values of $f_{31000}(s)$ are at the circles with radii equal to $|C_{t,\boldsymbol{m}}|$ as shown in Fig. 19.

APPENDIX B: AN EXAMPLE FOR THE CORRELATION BETWEEN THE RDT BUILD-UP FLUCTUATIONS AND DA AREA

Since the two kinds of RDT fluctuations are strongly related, minimizing the average amplitude of the RDT build-up fluctuations could also be effective in the DA optimization. Here the SSRF lattice is also used as an example, where the third-order RDTs are the main nonlinear terms. We use

$$h'_{3,\mathrm{ave}} = \sqrt{\sum_{j+k+l+m=3} \left(\sum_{t=1}^{N} |h_{1\to t,jklm0}|/N \right)^2} \quad \text{(B1)}$$

to quantitatively represent the build-up fluctuation of third-order RDTs. Figure 20 shows the correlation between $h'_{3,\mathrm{ave}}$, $h_{3,\mathrm{ring}}$ and DA area for the same solutions as in Fig. 7. We can clearly see that Fig. 20 is almost the same as Fig. 7(a). The correlation between $h'_{3,\mathrm{ave}}$ and $h_{3,\mathrm{ave}}$ can be measured by the Spearman rank-order correlation coefficient, r_s [42]. The coefficient r_s is a nonparametric measure of the monotonicity of the relationship between two datasets, which varies between -1 and $+1$ with 0 implying no correlation. The values -1 and $+1$ imply exact monotonic relationship. For $h'_{3,\mathrm{ave}}$ and $h_{3,\mathrm{ave}}$, r_s is 0.967, indicating a very strong correlation between the two kinds of RDT fluctuations. Therefore, minimizing the RDT build-up fluctuations is also effective in enlarging the DA. If the number of SPs of a ring is very small, it is better to calculate the RDT build-up fluctuations for multiple turns to have better convergence of calculation.

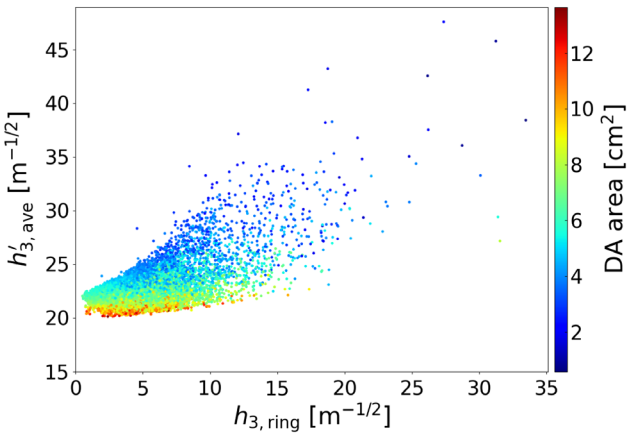

FIG. 20. Correlation between the average amplitude of the RDT build-up fluctuation $h'_{3,\mathrm{ave}}$, one-turn RDT $h_{3,\mathrm{ring}}$, and DA area for the SSRF lattice.

[1] M. Borland, L. Emery, V. Sajaev, and A. Xiao, Direct methods of optimization of storage ring dynamic and momentum aperture, in *Proceedings of the Particle Accelerator Conference (PAC09), Vancouver, BC, Canada* (JACoW, Geneva, 2009).

[2] L. Yang, Y. Li, W. Guo, and S. Krinsky, Multiobjective optimization of dynamic aperture, Phys. Rev. ST Accel. Beams **14**, 054001 (2011).

[3] W. Gao, L. Wang, and W. Li, Simultaneous optimization of beam emittance and dynamic aperture for electron storage ring using genetic algorithm, Phys. Rev. ST Accel. Beams **14**, 094001 (2011).

[4] Z. Bai, W. Li, and L. Wang, Enlarging dynamic and momentum aperture by particle swarm optimization, in *Proceedings of the International Particle Accelerator Conference (IPAC2011), San Sebastián, Spain* (JACoW Publishing, Geneva, 2011).

[5] X. Huang and J. Safranek, Nonlinear dynamics optimization with particle swarm and genetic algorithms for SPEAR3 emittance upgrade, Nucl. Instrum. Methods Phys. Res., Sect. A **757**, 48 (2014).

[6] M. P. Ehrlichman, Genetic algorithm for chromaticity correction in diffraction limited storage rings, Phys. Rev. Accel. Beams **19**, 044001 (2016).

[7] J. Bengtsson, The sextupole scheme for the Swiss Light Source (SLS): An analytic approch, SLS Report No. Note 9/97, 1997.

[8] J. C. Biasci, J. F. Bouteille, N. Carmignani, J. Chavanne, D. Coulon, Y. Dabin, F. Ewald, L. Farvacque, L. Goirand, M. Hahn, J. Jacob, G. LeBec, S. Liuzzo, B. Nash, H. Pedroso-Marques, T. Perron, E. Plouviez, P. Raimondi, J. L. Revol, K. Scheidt, and V. Serrière, A low-emittance lattice for the ESRF, Synchrotron Radiat. News **27**, 8 (2014), .

[9] A. Streun, T. Garvey, L. Rivkin, V. Schlott, T. Schmidt, P. Willmott, and A. Wrulich, SLS-2—the upgrade of the Swiss Light Source, J. Synchrotron Radiat. **25**, 631 (2018).

[10] R. Bartolini, Storage ring design for synchrotron radiation sources, in *Synchrotron Light Sources and Free-Electron Lasers*, 2nd ed. (Springer, Cham, 2020), pp. 296–316.

[11] F. Schmidt, A. Verdier, and D. Kaltchev, Robustness of resonance free lattices against gradient errors, in *Proceedings of the Particle Accelerator Conference (PAC2002), Chicago* (JACoW Publishing, Geneva, 2001).

[12] Y. Cai, K. Bane, R. Hettel, Y. Nosochkov, M.-H. Wang, and M. Borland, Ultimate storage ring based on fourth-order geometric achromats, Phys. Rev. ST Accel. Beams **15**, 054002 (2012).

[13] A. Streun, inside opa, https://ados.web.psi.ch/opa (2022).
[14] M. Benedikt, F. Schmidt, R. Tomás, P. Urschütz, and A. Faus-Golfe, Driving term experiments at cern, Phys. Rev. ST Accel. Beams **10**, 034002 (2007).
[15] A. Franchi, R. Tomás, and F. Schmidt, Magnet strength measurement in circular accelerators from beam position monitor data, Phys. Rev. ST Accel. Beams **10**, 074001 (2007).
[16] R. Tomás, M. Bai, R. Calaga, W. Fischer, A. Franchi, and G. Rumolo, Measurement of global and local resonance terms, Phys. Rev. ST Accel. Beams **8**, 024001 (2005).
[17] A. Franchi, L. Farvacque, F. Ewald, G. Le Bec, and K. B. Scheidt, First simultaneous measurement of sextupolar and octupolar resonance driving terms in a circular accelerator from turn-by-turn beam position monitor data, Phys. Rev. ST Accel. Beams **17**, 074001 (2014).
[18] M. Borland, ELEGANT: A flexible SDDS-compliant code for accelerator simulation, Tech. Rep. Advanced Photon Source LS-287 (Argonne National Lab., IL (US), 2000).
[19] Y. Li, K. Hwang, C. Mitchell, R. Rainer, R. Ryne, and V. Smaluk, Design of double-bend and multibend achromat lattices with large dynamic aperture and approximate invariants, Phys. Rev. Accel. Beams **24**, 124001 (2021).
[20] A. Chao, Lecture notes on topics in accelerator physics, Stanford Linear Accelerator Center Tech. Rep. No. SLAC-PUB-9574, 2002.
[21] G.-M. Liu, Z.-M. Dai, H.-H. Li, Y. Liao, Y. Xu, B.-C. Jiang, J. Hou, and Z.-T. Zhao, Lattice design for SSRF storage ring, High Energy Phys. Nucl. Phys. **30**, 144 (2006), http://cpc.ihep.ac.cn/article/id/1956c056-5b04-455e-8cbe-88232820576d.
[22] Jazzbin *et al.*, geatpy: The genetic and evolutionary algorithm toolbox with high performance in python (2020), http://www.geatpy.com/.
[23] S.-Q. Tian, G.-M. Liu, H.-H. Li, J. Hou, G.-L. Chen, and C.-L. Wan, Improved nonlinear optimization in the storage ring of the modern synchrotron radiation light source, Chin. Phys. C **33**, 65 (2009).
[24] L. Nadolski and J. Laskar, Review of single particle dynamics for third generation light sources through frequency map analysis, Phys. Rev. ST Accel. Beams **6**, 114801 (2003).
[25] R. Hettel, DLSR design and plans: an international overview, J. Synchrotron Radiat. **21**, 843 (2014).
[26] D. Einfeld, M. Plesko, and J. Schaper, First multi-bend achromat lattice consideration, J. Synchrotron Radiat. **21**, 856 (2014).
[27] J. Bengtsson and P. Tavares, Towards a Diffraction Limited Storage Ring, in *Proc. 10th International Particle Accelerator Conference (IPAC'19), Melbourne, Australia, 19-24 May 2019*, International Particle Accelerator Conference No. 10 (JACoW Publishing, Geneva, Switzerland, 2019) pp. 1573–1576, 10.18429/JACoW-IPAC2019-TUPGW075.
[28] A. Loulergue, D. Amorim, P. Brunelle, A. Gamelin, A. Nadji, L. Nadolski, R. Nagaoka, R. Ollier, and M.-A. Tordeux, CDR Baseline lattice for the upgrade of SOLEIL, in *Proceedings of the International particle Accelerator Conference (IPAC'21), Campinas, SP, Brazil* (JACoW Publishing, Geneva, Switzerland, 2021), pp. 1485–1488, 10.18429/JACoW-IPAC2021-TUPAB054.
[29] P. Yang, W. Li, Z. Ren, Z. Bai, and L. Wang, Design of a diffraction-limited storage ring lattice using longitudinal gradient bends and reverse bends, Nucl. Instrum. Methods Phys. Res., Sect. A **990**, 164968 (2021).
[30] Z. Ren, Z. Bai, J. Tan, L. Wang, H. Xu, and P. Yang, Complex unit lattice cell for low-emittance synchrotrons, in *Proc. IPAC'21* (JACoW Publishing, Geneva, Switzerland, 2021) pp. 3254–3256, 10.18429/JACoW-IPAC2021-WEPAB263.
[31] G. Baranov, A. Bogomyagkov, I. Morozov, S. Sinyatkin, and E. Levichev, Lattice optimization of a fourth-generation synchrotron radiation light source in Novosibirsk, Phys. Rev. Accel. Beams **24**, 120704 (2021).
[32] J. Bengtsson and A. Streun, Robust design strategy for SLS-2, Tech. Rep. No. SLS2-BJ84-001-2 (PSI, Villigen, Switzerland, 2017).
[33] Z. Bai, Lattice design progress of the HALF storage ring, in *3rd Workshop on Low Emittance Lattice Design, Barcelona, Spain,* (2022), https://indico.cells.es/event/1072/contributions/1787/.
[34] A. Terebilo, Accelerator Toolbox for MATLAB, Stanford Linear Accelerator Center Report No. SLAC-PUB-8732, 2001.
[35] Y. Li, W. Cheng, L. H. Yu, and R. Rainer, Genetic algorithm enhanced by machine learning in dynamic aperture optimization, Phys. Rev. Accel. Beams **21**, 054601 (2018).
[36] J. Wan, P. Chu, Y. Jiao, and Y. Li, Improvement of machine learning enhanced genetic algorithm for nonlinear beam dynamics optimization, Nucl. Instrum. Methods Phys. Res., Sect. A **946**, 162683 (2019).
[37] J. Wan, P. Chu, and Y. Jiao, Neural network-based multi-objective optimization algorithm for nonlinear beam dynamics, Phys. Rev. Accel. Beams **23**, 081601 (2020).
[38] L. Emery, H. Shang, Y. Sun, and X. Huang, Application of a machine learning based algorithm to online optimization of the nonlinear beam dynamics of the Argonne Advanced Photon Source, Phys. Rev. Accel. Beams **24**, 082802 (2021).
[39] M. Giovannozzi, E. Maclean, C. E. Montanari, G. Valentino, and F. F. Van der Veken, Machine learning applied to the analysis of nonlinear beam dynamics simulations for the CERN large hadron collider and its luminosity upgrade, Information **12**, 53 (2021).
[40] J. Wan and Y. Jiao, Machine learning enabled fast evaluation of dynamic aperture for storage ring accelerators, New J. Phys. **24**, 063030 (2022).
[41] S. C. Leemann and A. Streun, Perspectives for future light source lattices incorporating yet uncommon magnets, Phys. Rev. ST Accel. Beams **14**, 030701 (2011).
[42] S. W. Looney and J. L. Hagan, 2—statistical methods for assessing biomarkers and analyzing biomarker data, in *Essential Statistical Methods for Medical Statistics*, edited by C. R. Rao, J. P. Miller, and D. C. Rao (North-Holland, Boston, 2011) pp. 27–65.